RSC Advances

PAPER

View Article Online
View Journal | View Issue

Cite this: *RSC Adv.*, 2025, **15**, 10310

Detection of pesticide residue using an Fe_3O_4/GO/Ag nanocomposite as a SERS substrate and mechanism investigation†

Rui Wu, * Xi Song, Yulin Wang and Qiang Zhang

Considering that pesticide residues cause significant harm to health and the environment, it is crucial and urgent to fabricate surface-enhanced Raman scattering (SERS) substrates with high sensitivity to detect pesticide residues. In this study, a three-layer structure of multifunctional Fe_3O_4/GO/Ag nanoparticles (NPs) as an active substrate for SERS was fabricated and comprehensively characterized through X-ray diffraction (XRD), transmission electron microscopy (TEM), scanning electron microscopy (SEM), energy dispersive spectroscopy (EDS), elemental mapping, and X-ray photoelectron spectroscopy (XPS). The active substrate was used to detect thiram pesticide through SERS. Combined with the synergistic effect, Ag NPs and graphene oxide (GO) possessed high-density and ordered hot spots to enhance the electromagnetic field; therefore, signal amplification and fascinating sensitivity were achieved. The lowest concentration of thiram for clear presentation of the peak was 10^{-12} mol L^{-1}. There was a satisfactory linear relationship, ranging from 10^{-10} to 10^{-4} mol L^{-1}, with a low limit of detection, high sensitivity, satisfactory enhancement factor (EF), stability, and repeatability. In addition, Fe_3O_4/GO/Ag was successfully applied to identify pesticide residues in a practical sample. Furthermore, the enhancement mechanism, including electromagnetic enhancement and chemical reinforcement, is discussed in detail. Fe_3O_4/GO/Ag is a potential active substrate for SERS and can be applied for rapid detection in the food industry, environmental fields and biomedicine with fascinating sensitivity.

Received 14th February 2025
Accepted 15th March 2025

DOI: 10.1039/d5ra01081k

rsc.li/rsc-advances

1. Introduction

In modern agricultural production, an increasing number of pesticides are being used to control or eliminate pests to improve the quality and yield of crops. Although pesticide spraying benefits agricultural production, pesticide residues and their metabolites may contaminate and affect food products at all stages from production to consumption. These residues in food products may pollute the environment and pose a threat to the health of consumers.[1,2] Thiram belongs to the dithiocarbamate pesticide group, which is widely used to control the infestation of vegetables, fruits and pests. Thiram can be easily accumulated in crops.[3] Therefore, strengthening the detection of pesticide residues is of pivotal significance for the protection of the environment and human health.

Thus far, various techniques have been proposed for the detection of pesticide residues. For example, immunoassays and enzyme inhibition are rapid approaches with low detection cost, ease of operation and portable advantages but with low sensitivity and complex preparation of antibodies.[4] Gas chromatography, gas chromatography-mass spectrometry, high-performance liquid chromatography and other precision instrumental methods are also often used to monitor pesticide residues.[5–7] Although the reported methods have made great progress, some are time-consuming with complex operation and, more importantly, low sensitivity, which hinder their development and universality. Therefore, it is urgent to develop a novel approach to detect pesticide residue with high sensitivity and universality.

As an emerging spectroscopic technique, SERS is widely used in the fields of food safety, biosensing, and environmental detection owing to its high sensitivity, low damage to the sample, and ability to provide comprehensive fingerprint information.[8–10] SERS is a potential tool to detect a variety of pesticide species with the aid of active SERS substrates. To achieve high sensitivity and trace detection, highly active substrates with signal enhancement are required, and noble metal nanoparticles are often employed as active substrates for SERS detection.[11,12] It has been reported that the composition, particle size and morphology of the substrate affect the generation and intensity of the Raman signal of the analyte.[13,14] Nanoparticles of noble metals, such as Ag, Au, Pt and Cu substrates have a high density of hot-spot regions, especially Ag NPs.[15,16] Ag NPs produce the strongest SERS effect, which has

Shaanxi Province Key Laboratory of Catalytic, School of Chemical and Environmental Science, Shaanxi University of Technology, Hanzhong 723001, P. R. China. E-mail: hftffc@163.com; wurui@snut.edu.cn

† Electronic supplementary information (ESI) available. See DOI: https://doi.org/10.1039/d5ra01081k

great potential for the detection of trace pollutants.[17] For example, Vu reported the trace detection of ciprofloxacin using silver nanostars as SERS substrates.[18] Dowgiallo used Au nanoparticles as SERS substrates to determine the detection limits of various pesticides.[19] However, poor stability and sensitivity are the biggest drawbacks of single precious metal substrates, and they have limitations in practical applications. Nowadays, the preparation of composite substrates has overcome the shortcomings and implemented the concept of sustainable development. Fe_3O_4 nanoparticles have received widespread attention owing to their ease of separation, simple synthesis and chemical stability.[20] Yang's and Han's group prepared core–shell Fe_3O_4@Ag and Fe_3O_4@Au composites, respectively, as recyclable magnetic SERS substrates for thiram detection.[21,22] As a multifunctional material, graphene has received extensive attention by researchers for its unique structure and excellent electrical and optical properties. Graphene mainly provides chemical enhancement in the Raman enhancement process, and it has a highly conjugated system. Because graphene is enriched in surface molecules through Π–Π stacking effect synergized with non-covalent bonding forces, it enhances the adsorption effect of most SERS substrates and guarantees the sensitivity and accuracy for the detection of target molecules.[23,24] A composite substrate overcomes the shortcomings of a single substrate and combines the advantages of its individual components, extending the application of SERS in the field of food safety analysis.

In this study, a three-layer SERS substrate, Fe_3O_4/GO/Ag, was fabricated. Based on the adsorption of the composite SERS substrate onto the target molecules, quantitative detection of thiram was achieved, as depicted in Scheme 1. The composite nanomaterial substrate Fe_3O_4/GO/Ag combines the excellent adsorption properties of graphene oxide (GO), the unique magnetic properties of Fe_3O_4, and the hot spot of Ag, providing new insights and a platform for the detection of pesticide residues.

2. Materials and methods

2.1 Chemicals and materials

Graphite powder was obtained from Tianjin Damao Chemical Reagent Factory. Concentrated sulfuric acid, sodium nitrate, hydrogen peroxide, potassium permanganate, ferric chloride, silver nitrate, acetone and ferrous sulfate were purchased from Sinopharm Chemical Reagent Co. 3-Aminopropltriethoxysilane (APTES), tri-hydroxymethyl aminomethane, dopamine hydrochloride were obtained from Aladdin. All chemicals were of analytical grade, and deionized water was prepared using the millipore water purification system.

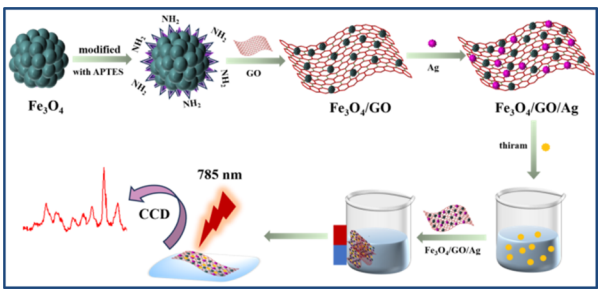

Scheme 1 Illustration of the fabrication process of Fe_3O_4/GO/Ag with its application in SERS.

2.2 Preparation of the SERS substrate

2.2.1 Synthesis of Fe_3O_4. A three-necked flask was filled with 50.0 mL of deionized water under mechanical stirring, and nitrogen was passed to remove oxygen for at least 30 min. Then, 0.3336 g of ferrous sulfate (1.2 mmol) and 0.6487 g of ferric trichloride (2.4 mmol) were added to the three-necked flask, and the temperature of the water bath was maintained at 60 °C. The solids were completely dissolved, and the solution turned orange-yellow. The pH of the solution was adjusted to 9.0–10.0 using ammonia, and the solution colour changed rapidly from orange to black, and the reaction continued for 30 min. Subsequently, stop stirring. The temperature of the water bath was raised to 85 °C and the mixture was aged for an additional 30 min. The nitrogen was maintained continuously throughout the process.[25] The solution was then cooled to room temperature and washed alternately with deionized water and anhydrous ethanol until it became neutral. The product was dried in an oven at 60 °C and preserved for subsequent application.

2.2.2 Synthesis of GO. Graphite powder (1.0001 g) and sodium nitrate (0.5005 g) were dissolved in 40 mL of concentrated sulfuric acid and stirred for 30 min in an ice bath (5 °C).[26] Potassium permanganate (5.0125 g) was divided into ten parts and added slowly to the above mixture, and the reaction was continued for 60 min. The temperature was then increased to 35 °C and maintained for 60 min, after which 50 mL of deionized water was slowly added. The temperature of the water bath was adjusted to 80 °C and maintained for 30 min, and next, the three-necked flask was removed. Subsequently, 50 mL of deionized water and 30% hydrogen peroxide were added to the solution until no bubbles were formed. A golden yellow solution was obtained. The solution was subjected to centrifugal separation, followed by washing the precipitate thrice with a hydrochloric acid solution and then with deionized water until the precipitate turned neutral. A yellowish-brown product was obtained. The obtained graphene oxide was dried in a vacuum oven at 35 °C and stored for future use.

2.2.3 Synthesis of Fe_3O_4/GO. Fe_3O_4 (0.4122 g) was dispersed in 20 mL of isopropanol and dissolved *via* ultrasonication for 40 min. Then, 0.12 mL of APTES was slowly added dropwise, and the mixture was transferred to a flask and refluxed at 85 °C for 3 h.[27] Subsequently, the flask was removed from the water bath and cooled to room temperature. Magnetic separation was performed with the aid of magnets, and the free APTES was washed with ethanol and deionized water. The obtained product was completely dispersed in 35 mL of deionized water. GO (0.0687 g) was accurately weighed and dispersed in 35 mL of deionized water. The two types of solutions were mixed and dispersed homogeneously *via* ultrasonication for 30 min, followed by stirring at room temperature overnight. Solid Fe_3O_4/

GO nanoparticles were obtained using magnetic separation with magnets. They were washed several times with ethanol and deionized water and dried in a vacuum at 60 °C.

2.2.4 Synthesis of Ag NPs. Sodium citrate (0.0183 g) and silver nitrate (0.0106 g) were added to a 250 mL volumetric flask containing deionized water. In a beaker, 100 mL of the above-mixed solution and 0.2 mL of a PVP (1%) solution was added, and the mixture was stirred at room temperature for 20 min. Then, 1 mL (0.01 M) of ascorbic acid (AA) solution was added. After 15 min, gray-green Ag sol was obtained.[28]

2.2.5 Fabrication of Fe_3O_4/GO/Ag nanocomposites. Tris–HCl solid (0.12 g) was dissolved in 100 mL of deionized water, and the pH of the solution was adjusted to 8.5 with HCl. Tris–HCl buffer solution was prepared. Dopamine hydrochloride solid (0.3 g) and Fe_3O_4/GO (0.2 g) were weighed separately and added to the newly prepared 90 mL of Tris–HCl buffer solution, and the resulting solution was subjected to ultrasonication for 30 min and stirred overnight at room temperature.[29] The solution was magnetically separated, washed several times with deionized water and anhydrous ethanol, and dried under vacuum at 60 °C.

Amino-functionalized Fe_3O_4/GO (0.1 g) was weighed in a beaker, and 25 mL of deionized water was added and ultrasonically dispersed uniformly. Then, 20 mL of Ag sol was added, ultrasonically dispersed for 15 min, and then left undisturbed for 15 min for magnetic separation. To load a large amount of Ag NPs on Fe_3O_4/GO, the same operation was repeated 10 times. The final products were washed with ethanol and dried in a vacuum drying oven at 60 °C to obtain Fe_3O_4/Ag.

2.3 Characterization

The X-ray diffraction (XRD) pattern was recorded on a D8 ADVANCE X-ray diffractometer. UV-visible (UV-vis) spectrophotometry (Shimadzu's Uv-2600) and infrared (IR) spectrometry (Bruker's Vertex 70) were used to obtain the UV-visible absorption peaks and infrared characteristic peaks, respectively, of the prepared materials. The structure and morphology were investigated through transmission electron microscopy (TEM) with FEI Tecnai G2 S-Twin. X-ray photoelectron spectroscopy (XPS, Kratos Axis ULTRA) was conducted. Raman spectroscopy was performed using a confocal microscope Raman spectrometer system (Horiba, LabRAMHR). The Raman spectra of GO and thiram were obtained under different experimental parameters.

2.4 Application of the active substrate

2.4.1 SERS performance of the active substrate. Preparation of the working curve: 0.1213 g of thiram powder was taken in a 50 mL volumetric flask dissolved in acetone *via* ultrasound treatment to obtain 10^{-2} mol L^{-1} of mother solution. The mother solution was diluted with deionized water to obtain a series of concentrations of thiram (10^{-4}–10^{-10} mol L^{-1}) as a standard solution to plot the working curve.

Preparation of the thiram sample based on the Fe_3O_4/GO/Ag substrate: 1 mg of Fe_3O_4/GO/Ag was added to 500 μL of different concentrations of thiram standard solutions with sonication for even dispersion. Next, 30 μL of the test sample was placed on a slide and dried at room temperature for SERS detection. All tests were conducted in at least triplicate.

Test conditions: Raman measurements were conducted under ambient conditions with a 785 nm wavelength as the excitation source. The integration time per spectrum was 10 s, the laser power of the excitation source was 50 mW and the scanning range was from 400 to 1600 cm^{-1}.[30]

2.4.2 Detection of thiram in real samples. To verify the feasibility of the proposed method for application, tap water, pear juice and apple juice spiked with different amounts of thiram were analysed. Apples and pears purchased from the market were washed, crushed and squeezed. Ethanol (1 mL) was added to the juice, which was ultrasonicated and shaken for 10 min, transferred to a centrifuge tube, and then centrifuged for 15 min at 8000 rpm.[31] The supernatant was used as the test solution to acquire Raman signals.

3. Results and discussion

3.1 Characterization of Fe_3O_4/GO/Ag nanocomposites

The XRD patterns of the prepared Fe_3O_4, Fe_3O_4/GO and Fe_3O_4/GO/Ag NPs are shown in Fig. 1(a). As shown in Fig. 1(a), 2θ = 30.1°, 35.4°, 43.2°, 53.4°, 57.1°, and 62.8° are the diffraction peaks of the green Fe_3O_4 nanomaterial solution, which correspond to the six crystallographic diffraction peaks of (220), (331), (400), (511), (440), and (531), respectively, of the crystal structure of Fe_3O_4, and were identical to the diffraction peaks of the standard card (JCPDS no. 1901-0629).[32,33] These results indicate that Fe_3O_4 was successfully synthesized. 2θ = 12° corresponds to the GO in Fe_3O_4/GO, represented with a red line, which coincides with reported values.[34] For Fe_3O_4/GO/Ag nanomaterials, in addition to the peaks of Fe_3O_4 and GO, the spectrum exhibited apparent diffraction peaks at 2θ = 38.1°, 44.2°, 64.3°, and 77.5°, given as the blue line, which were attributed to cubic Ag NPs, with reflections from (111), (200), (220), and (311), respectively.[35] Compared with the three lines, the intensity of Fe_3O_4 diffraction peaks was stronger than that of Fe_3O_4/GO and Fe_3O_4/GO/Ag composites because, probably, the GO and Ag on the surface of Fe_3O_4 weaken its magnetism. In combination with other analyses, it can be concluded that GO and Ag were coated on the surface of Fe_3O_4. The real image of the prepared Fe_3O_4/GO/Ag powder is presented in the ESI.†

The IR of Fe_3O_4, GO, and Fe_3O_4/GO are shown in Fig. 1(b). There was an obvious absorption band located at 560 cm^{-1}, which was the characteristic absorption peak of the Fe–O bond on the surface of Fe_3O_4, given as the blue line. The absorption peaks located at 1041 cm^{-1} and 897 cm^{-1} were attributed to the stretching vibration of the epoxy group C–O–C on GO, represented with the red line. The absorption peak located at 3438 cm^{-1} corresponds to the peak of the stretching vibration of –OH, which indicated an abundance of GO oxygen-containing functional groups. It was beneficial to stabilization of the prepared composites in water and enrichment of the adsorbed material.[36] Considering the spectral line of Fe_3O_4/GO, given in black, in addition to the characteristic absorption band of Fe_3O_4, the peak at 1638 cm^{-1} was attributed to the stretching vibration of –C=O in the amide bond (–CONH). The wavelength

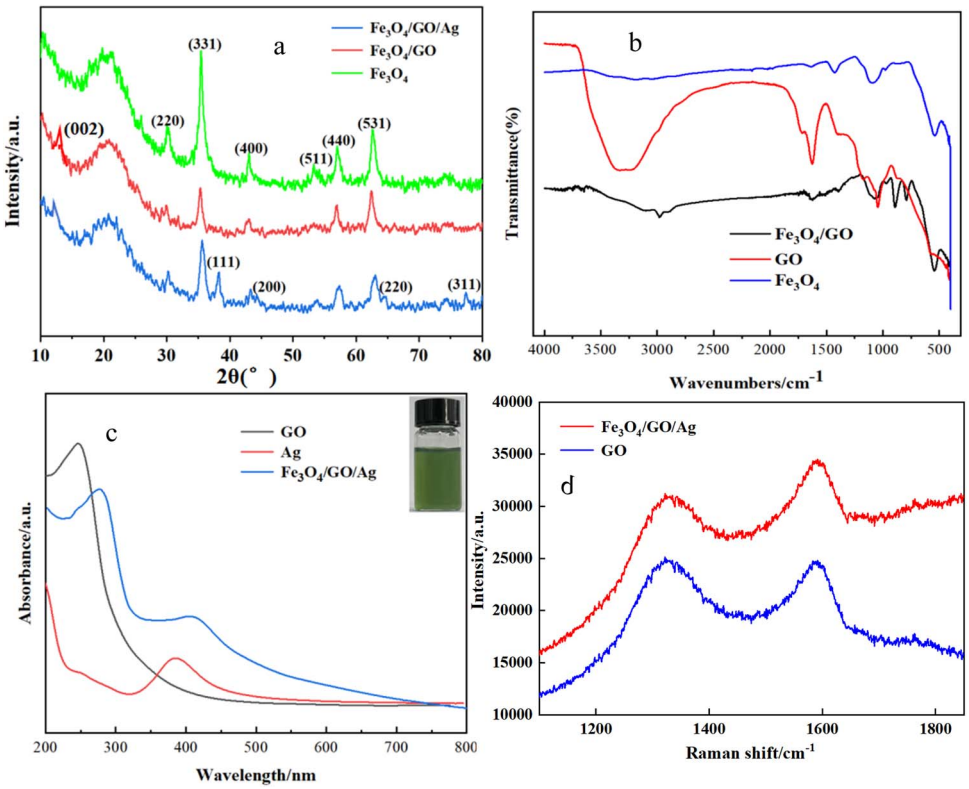

Fig. 1 (a) XRD patterns of Fe_3O_4, GO, and Fe_3O_4/GO; (b) IR of Fe_3O_4, GO, and Fe_3O_4/GO; (c) ultraviolet-visible absorption spectra of each sample (insert: silver nanosol); and (d) Raman spectra of GO in blue line and Raman spectra of Fe_3O_4/GO/Ag in red line.

at 1410 cm^{-1} was the stretching vibration peak of C–N in the amide bond, which indicated that GO was successfully loaded on Fe_3O_4.[37]

Fig. 1(c) shows the UV-visible absorption spectra of Ag, GO, and Fe_3O_4/GO/Ag. According to literature reports, Fe_3O_4 has no characteristic absorption peak in the UV-visible region. As shown in Fig. 3, the absorption peak at 240 nm was attributed to the distinct characteristic of GO, which is the π–π transition of conjugated C=C on GO. GO was successfully prepared using the Hummers' method. The location of the resonance peaks in the UV-vis absorption spectra of Ag NPs is subject to change with the particle size and morphology. In Fig. 3, a significant absorption peak band around 390 nm, represented as a red line, was observed, which was consistent with the UV-visible characteristic absorption peaks of Ag NP.[38,39] Compared with the synthesized pure GO and Ag nanoparticles, the absorption peaks of GO and Ag in Fe_3O_4/GO/Ag showed little positional shifts, and their absorption peaks appeared as broader peaks at 280 nm and 420 nm. Perhaps the loading of GO and Ag caused a red shift due to plasmonic resonance.

Raman spectroscopy is a powerful tool for characterizing carbon materials. Raman spectra of GO and Fe_3O_4/GO/Ag are shown in Fig. 1(d). Graphite can be oxidized by potassium permanganate into graphene oxide, and the graphite lamellae were ring-broken after oxidation, with a decrease in the degree of regularity and an increase in the degree of defects. According to the literature, the D and G peaks are Raman characteristic peaks of carbon atom crystals, in which the D peak represents the defects of carbon atom crystals, which usually appear in the range of 1300–1400 cm^{-1}, and the G peak represents the symmetry and orderliness of the graphite structure, which usually appears in the range of 1560–1620 cm^{-1}. The ratio of peak intensity between D and G peaks (I_D/I_G) is commonly used in Raman analysis to represent the disorder of graphite. The larger the ratio, the greater the disorder, the more the defects, and the higher the degree of oxidation of the material. Fig. 4

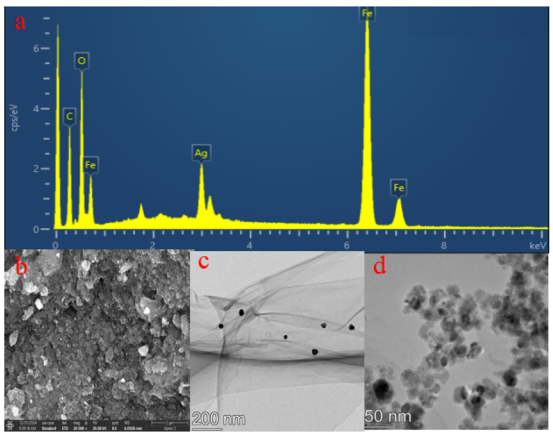

Fig. 2 EDS of Fe_3O_4/GO/Ag (a); SEM (b) and TEM images of Ag (c); TEM image of Fe_3O_4/GO/Ag (d).

shows significant Raman characteristic peaks at 1330 and 1592 cm^{-1} with $(I_D/I_G) = 0.90$, much higher than graphite $I_D/I_G = 0.14$, indicating that graphite was fully oxidized and exfoliated to produce GO.[40,41] Comparing the two sets of Raman spectra, it was found that graphene oxide and Fe_3O_4/GO/Ag had clear GO characteristic peaks.

The Fe, O, C and Ag elements were accurately identified using EDS (Fig. 2(a)), as well as SEM and TEM imaging of Fe_3O_4/GO/Ag (Fig. 2(b) and (d)). Fig. 2(d) shows that the most obvious part was dark black Ag NPs due to their high atomic number, and they were round-shaped, which was consistent with the TEM image of Ag (Fig. 2(c)). Fe_3O_4 was dark gray, whereas GO was greyish with a thin film. The particle sizes of Ag and Fe_3O_4 were less than 50 nm. The mapping of individual elements and Fe_3O_4/GO/Ag are shown in Fig. 3(a) and (b). In summary, we successfully prepared Fe_3O_4/GO/Ag.

The chemical compositions of Fe_3O_4/GO/Ag were comprehensively analyzed through XPS, as shown in Fig. 4. The presence of iron (Fe), carbon (C), and oxygen (O) elements in the substrate is visible (Fig. 4(a)). The $2p_{1/2}$ and $2p_{3/2}$ peaks of Fe are observed at binding energies of 724.2 eV and 711.1 eV (Fig. 4(b)), respectively, which distinctly correspond to the characteristics of Fe_3O_4. For C 1s spectra, binding energies at 286.8 eV and 284.9 eV are attributed to the presence of different chemical states of carbon, namely, the C–O–C and C–C or C=C bond, respectively (Fig. 4(c)). Furthermore, C–O at 532.3 eV and H–O at 530.5 eV confirmed the presence of O 1 s in GO (Fig. 4(d)). The double peaks of Ag 3d, including Ag $3d_{5/2}$ at 368.2 eV and Ag $3d_{3/2}$ at 374.2 eV, were consistent with the standard binding energy (Fig. 4(e)). The combination of the analysis and unique magnetic separability exhibited by the products fully demonstrated the successful fabrication of Fe_3O_4/GO/Ag NPs.

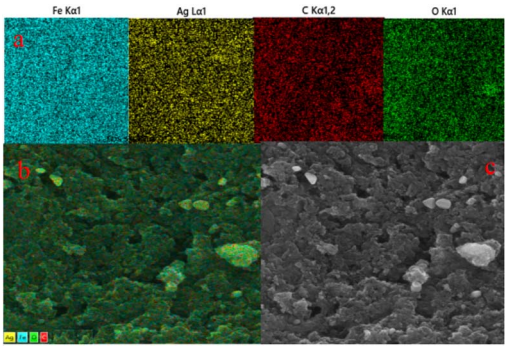

Fig. 3 (a) Color mapping of individual elements; (b) mapping and (c) SEM image of the same part of Fe_3O_4/GO/Ag.

3.2 SERS detection of thiram

Thiram as the target was analyzed in detail. Different concentrations of the thiram standard solution were mixed with the prepared active substrate, followed by Raman detection. Fig. 5 shows the Raman spectra of thiram based on Fe_3O_4/GO/Ag as the substrate. There were obvious characteristic bands at 432 cm^{-1}, 565 cm^{-1}, 745 cm^{-1}, 956 cm^{-1}, 1140 cm^{-1}, 1381 cm^{-1}, 1447 cm^{-1}, and 1536 cm^{-1}, which can be employed as the main Raman characteristic peaks of thiram. Among them, the band at 432 cm^{-1} was attributed to the bending vibration of CH_3CN and the stretching vibration of C=S in the molecular structure of thiram. The band at 565 cm^{-1} was attributed to S–S stretching vibration, and the band at 956 cm^{-1} was attributed to the vibrational peak of CH_3N. The band at 1140 cm^{-1} belong to C–N stretching vibration. The band at 1381 cm^{-1} was attributed to C–N stretching vibrations and CH_3 symmetric deformation. The peak at 1447 cm^{-1} was an antisymmetric peak of CH_3.[42,43] The peak locations were consistent with those reported in the literature. Thiram was completely

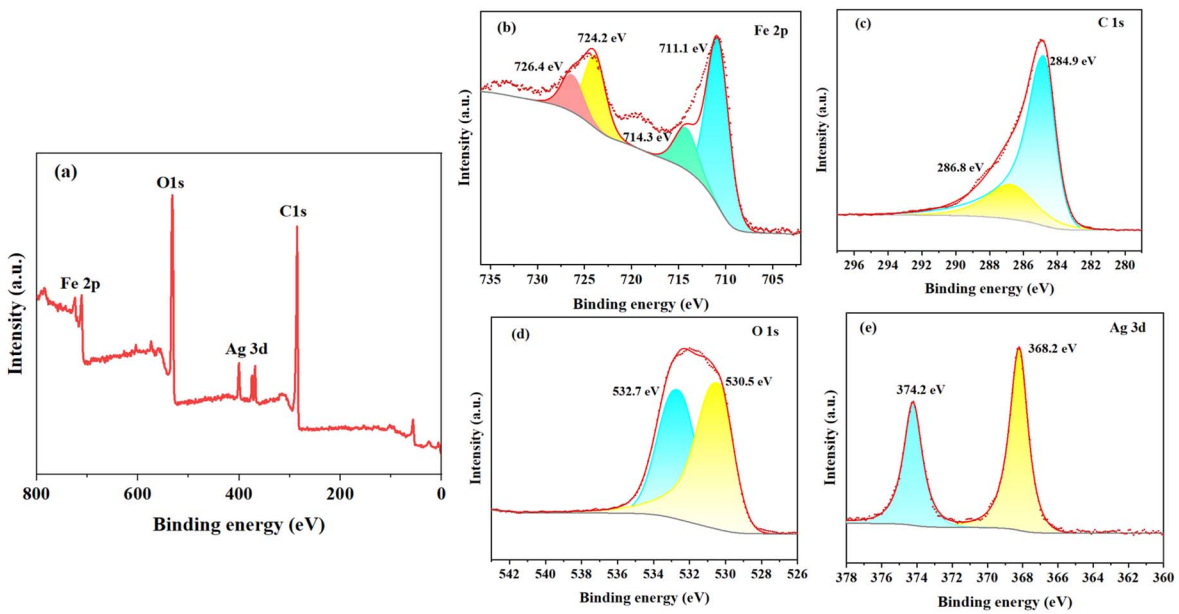

Fig. 4 (a) XPS spectrum of Fe_3O_4/GO/Ag and high-resolution XPS of (b) Fe, (c) C, (d) O, and (e) Ag.

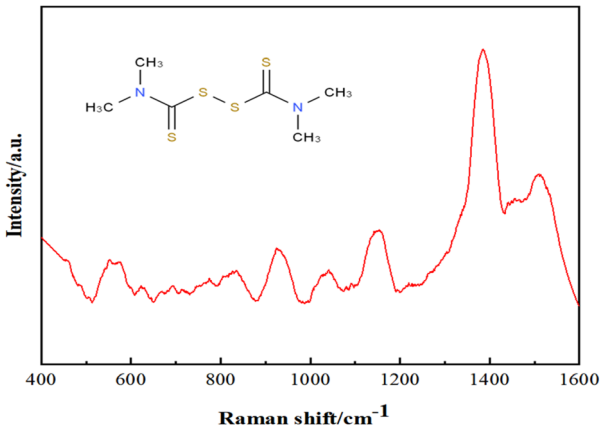

Fig. 5 Raman spectra of thiram.

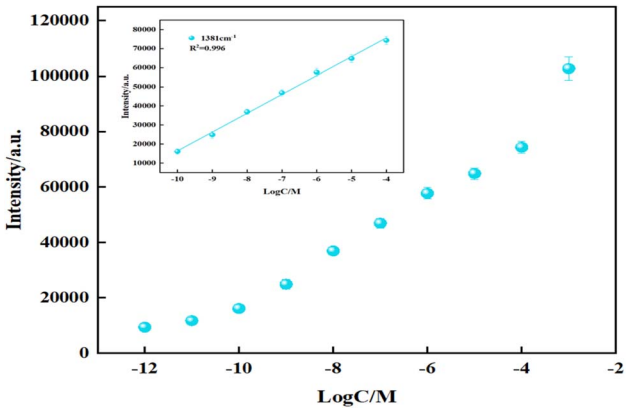

Fig. 7 Corresponding calibration plot of Raman intensity *versus* concentrations of thiram.

different from GO in terms of the test conditions and parameters of SERS. Thus, it avoided interference from GO.

Based on the constructed SERS substrate, the intensities of Raman characteristic peaks of different concentrations are shown in Fig. 6. The intensity of the characteristic peak at 1381 cm^{-1} is more obvious and enhanced with the increase in the concentration of thiram, ranging from 1×10^{-12} to 1×10^{-3} mol L^{-1}, which was therefore taken as the characteristic peak for thiram detection. To further correct the fluctuation of the Raman signal of thiram due to laser instability and substrate inhomogeneity during the detection process, the intensity of thiram at 1381 cm^{-1} with different concentrations was used to construct a working curve for the subsequent quantitative detection and analysis of thiram. As shown in Fig. 7, the standard curve showed perfect linearity in the range of 1×10^{-10}–1×10^{-4} mol L^{-1}, with a correlation coefficient (R^2) of 0.9960, and the optimal fitting equation was $Y = 9876 \log X + 115\,162$. Although there were obvious signals for 1×10^{-11} and 1×10^{-12} mol L^{-1} of thiram, they seem nonlinear (Fig. 8).

3.3 Detection of thiram in real samples

We put the proposed methodology into practice. Tap water, apple juice and pear juice as samples were exploited to investigate the spiked recovery experiments. The added amounts of thiram in tap water and fruit juice were 2×10^{-10}, 5×10^{-10} and 1×10^{-9} M. As shown in Table 1, the average recovery was 90.2–104.2%. These results indicated that the sensor has great promise for the detection of thiram and other analytes in agriculture, food, medicine and environmental safety.

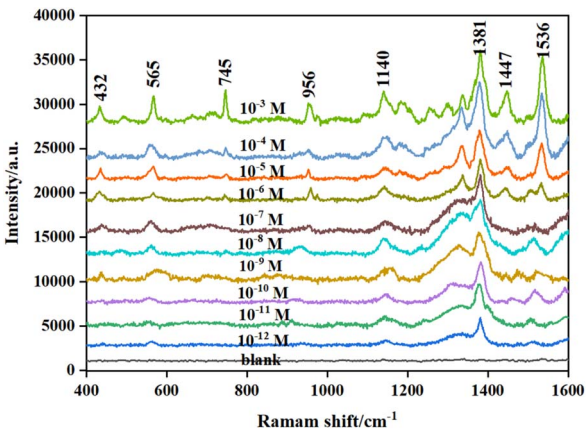

Fig. 6 Raman spectra for different concentrations of thiram.

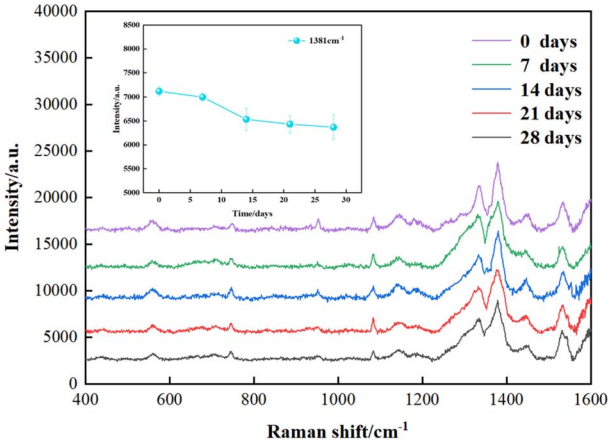

Fig. 8 SERS spectra of 10^{-4} M thiram using Fe_3O_4/GO/Ag as substrate that has been stored for various periods.

Table 1 Results of recovery experiments for detecting thiram in real samples

Samples	Spiked (M)	Recovery (%)
Pear juice	1×10^{-9}	103.8
	5×10^{-10}	98.7
	2×10^{-10}	92.9
Apple juice	1×10^{-9}	103.3
	5×10^{-10}	104.2
	2×10^{-10}	90.2
Tap water	1×10^{-9}	101.9
	5×10^{-10}	98.4
	2×10^{-10}	97.2

3.4 Activity, stability and repeatability of Fe_3O_4/GO/Ag

EF was estimated using the following equation: $EF = I_{SERS} \times C_0 / I_0 \times C_{SERS}$; here, I_0 and I_{SERS} are the intensities of the normal Raman and intensities of SERS with Fe_3O_4/GO/Ag as substrate, respectively. C_{SERS} and C_0 are the concentrations of the mixed thiram with Fe_3O_4/GO/Ag and bare thiram. The EF for thiram at 1381 cm^{-1} was 2.8×10^8. This may be attributed to two types of enhancement mechanisms: electromagnetic enhancement mechanism (EM) and chemical enhancement mechanism (CM).

In this study, the minimum visible signal was achieved for 10^{-12} mol L^{-1} of thiram. If the concentration of thiram is lower than 10^{-12} mol L^{-1}, no detectable signal is obtained. Meanwhile, the formulation ($LOD = 3\delta/k$) was employed to calculate the limit of detection (LOD), where δ is the standard deviation of the blank and k is the slope of the calibration curve. At 1381 cm^{-1}, the LOD is $10^{-11.7}$ mol L^{-1}. The two results nearly coincide. To verify the stability of Fe_3O_4/GO/Ag, time-dependent SERS measurements were performed, as shown in Fig. 11 and 9. The intensity of the SERS signal did not substantially change over one month. The results showed that Fe_3O_4/GO/Ag was stable during preservation. In addition, repeatability plays an important role in SERS. To assess the repeatability of Fe_3O_4/GO/Ag, three samples were analyzed under the same conditions at 11 random locations on the substrate. High repeatability with a low RSD of approximately 5.1% was obtained, as shown in Fig. 10. The comparison of different materials for detection of thiram by SERS is presented in ESI.†

3.5 Exploration of the enhancement mechanism

In this study, a high EF of 2.8×10^8 for thiram was obtained at 1381 cm^{-1}. It is necessary to investigate the enhancement mechanism. Generally, it includes electromagnetic enhancement and charge transfer enhancement. However, electromagnetic enhancement is the main contribution. Electromagnetic enhancement means that owing to the local surface plasmon resonance (LSPR) effect of Ag, the electromagnetic field will be enhanced in the region of 10 nm on the surface of Ag.[44,45]

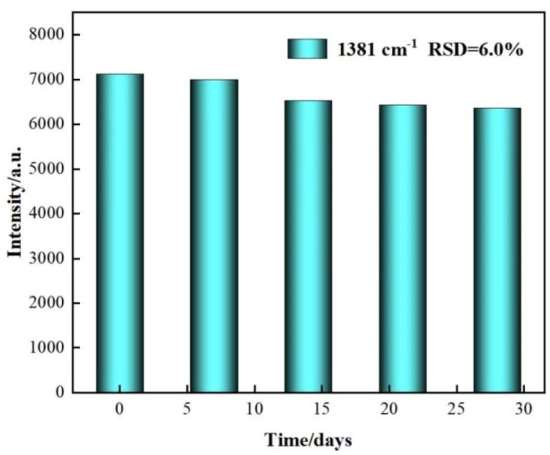

Fig. 9 SERS spectra of 10^{-4} M thiram at various periods.

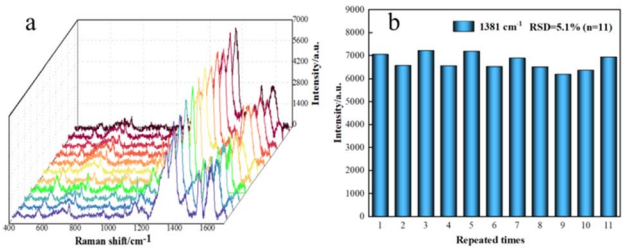

Fig. 10 (a) SERS spectra of 10^{-4} M thiram from 11 randomly selected Fe_3O_4/GO/Ag composite microspheres. (b) Raman intensity distribution of 1381 cm^{-1} peak from the 11 spectra.

Specially, when Ag NPs are excited by a specific wavelength of light, LSPR occurs on their surface. The resonance generates highly localized strong electromagnetic fields on Ag NPs, which significantly enhance the Raman signal of thiram adsorbed on the surface of the NPs. In addition, the lightning rod, antenna and mirror image models can explain LSPR enhancement. The tip of Ag NPs was treated as a perfect electrical conductor with a shape needle tip and it is similar to a slender wire. When an incident light was irradiated on the tip of Ag, a strong local electromagnetic field formed near the tip due to the small curvature radius of the tip. This local electromagnetic field interacted with thiram adsorbed near the tip of Ag, resulting in an enhanced Raman signal. The strongly enhanced field in the region of 10 nm is called a hot spot. If thiram is in the hot region, the Raman signal will amplify sharply. In this study, the coordination between Ag and thiram with sulfydryl shortens the distance between the substrate and target molecule, which may be in the hot spot. Furthermore, because of the aggregation of Fe_3O_4 and the adsorption property of GO, it endows Fe_3O_4/GO/Ag with enrichment ability. Therefore, the electromagnetic field intensity increased in the region of the hot spot, and the Raman signal amplified.

The chemical enhancement mechanism mainly includes resonance Raman enhancement, ground state chemical enhancement and charge transfer enhancement. Among them, charge transfer enhancement is generally approved. Charge transfer enhancement indicates that when incident light irradiates the surface of Ag and the semiconductor (GO), if the Fermi energy level of the surface is between the lowest unoccupied molecular orbital (LUMO) and the highest occupied molecular orbital (HOMO) of thiram, the energy of incident light matches charge transfer, and resonance Raman scattering occurs.[46,47] The free electrons on the surface of Ag and GO resonate and transit to the adsorbed thiram. These changes can significantly increase the polarizability of thiram. Meanwhile, the chemical bonding between thiram and Ag NPs can alter the vibration frequencies of thiram. Thus, the Raman signal of thiram is enhanced. In this study, because of the tunable band gap and distinctive charge transfer capability of GO, GO has been widely used as a SERS substrate. The excitation of electrons from the bands of GO to the LUMO of thiram is shown in Fig. 11. In brief, owing to Ag and GO, as well as Fe_3O_4, with the aid of electromagnetic fields and charge transfer, the Raman signal was enhanced.

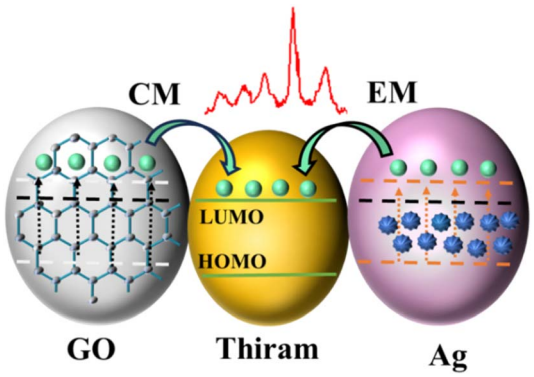

Fig. 11 Schematic of the CM and EM enhancement mechanisms.

4. Conclusion

In this study, a novel and ultra-high sensitive approach for detection of pesticide residues based on SERS was developed. The synthesized magnetic Fe_3O_4/GO/Ag nanohybrid was used as a SERS active substrate for Raman detection of thiram molecules. Fe_3O_4 was synthesized using a co-precipitation method, and modified Hummers-prepared graphene was employed to form Fe_3O_4/GO using a silane coupling agent as a bridge. The Fe_3O_4/GO/Ag nanohybrid as the active substrate was obtained through amino chemical modification of their surfaces for adsorption of Ag NPs. Its crystalline shape and structure were characterized. Results showed that Fe_3O_4/GO/Ag composites were successfully fabricated. With its feasible synthesis, Fe_3O_4/GO/Ag was successfully applied for thiram detection. It showed a notable linear relationship (10^{-10}–10^{-4} mol L^{-1}) and an R^2 of 0.9960. The designed Fe_3O_4/GO/Ag exhibited excellent enhancement with a high EF. Promising results were obtained for thiram detection in environmental samples. The established method is supersensitive, rapid and convenient with a wide linear range, low detection limit, low consumption, and ease of operation. Therefore, the magnetic nanohybrid as SERS the active substrate can not only improve the sensitivity and accuracy of pesticide residues, but can also have broad application prospects in real samples. The proposed method provides new insights for more rapid, sensitive and accurate detection. As a representative of a precious metal nanohybrid with magnetism, it is a promising active substrate, probe and photocatalyst. Moreover, it is of great significance for applications in the food industry, agriculture, industry, biomedicine and environmental fields.

Data availability

All data generated or analyzed during this study are included in this published article (and its ESI).†

Author contributions

R. Wu: conceptualization, data curation, funding acquisition, project administration, validation, editing, review, supervision, and draft methodology. X. Song: investigation, writing original. Y. L. Wang and Q. Zhang: formal analysis.

Conflicts of interest

The authors declare no conflict of interest.

Acknowledgements

This work was supported by the Key Research and Development Plan of Shaanxi Province (2024GX-YBXM-318), Graduate Education and Teaching Reform Project of Shaanxi University of Technology (SLGYKS2401), College Student Innovation and Entrepreneurship Project of Shaanxi University of Technology (202410720020), the Shaanxi Province Education Ministry Research Key Foundation (20JS015) and National Natural Science Foundation of China (22177066).

References

1 L. Lu, L. Xu, Y. Zhang Y, *et al.*, *Appl. Surf. Sci.*, 2022, **603**, 154419–154429.
2 K. S. Patel, P. K. Pandey and P. M. Ramos, *RSC Adv.*, 2023, **13**, 14914–14929.
3 S. Salam, A. Arif and R. Mahmood, *Pestic. Biochem. Physiol.*, 2020, **164**, 14–25.
4 W. Liu, Z. Z. Cong, G. C. Liu, *et al.*, *Inorg. Chim. Acta*, 2021, **527**, 120592–120599.
5 Y. Pico, H. Alfarhan and D. Barcelo, *Trends Anal. Chem.*, 2020, **122**, 115720–115753.
6 I. Dominguez, R. R. Gonzalez, F. G. A. Libanas, *et al.*, *Trends Environ. Anal. Chem.*, 2016, **12**, 1–12.
7 H. Zhang, Y. Yuan, Y. Sun, *et al.*, *Analyst*, 2018, **143**, 175–181.
8 M. Fan, G. Andrade and A. A. Brolo, *Anal. Chim. Acta*, 2020, **1097**, 1–29.
9 L. Jiang, M. Hassan, S. Ali, *et al.*, *Trends Food Sci. Technol.*, 2021, **112**, 225–240.
10 T. N. Wu, S. Yang and W. Feng, *Microchem. J.*, 2024, **198**, 110208–110213.
11 H. P. Zhou, J. Y. Qiu and Y. H. Zhang, *J. Hazard. Mater.*, 2024, **24**, 133868–133874.
12 Q. Zhang, R. Wu and C. F. Liu, *Rare Met. Mater. Eng.*, 2024, **53**, 546–554.
13 F. Selimoğlu and E. A. Muhammed, *Vib. Spectrosc.*, 2023, **126**, 103539–103545.
14 N. R. Barveen, J. L. Xu and Y. W. Cheng, *J. Environ. Chem. Eng.*, 2024, **12**, 112200–112206.
15 J. Y. Li, M. Li and Q. Q. Wang, *Spectrochim. Acta, Part A*, 2024, **311**, 124037–124043.
16 R. Wu, Q. C. Du, H. R. Zhang, *et al.*, *J. Saudi Chem. Soc.*, 2024, **28**, 101824–101837.
17 R. Wu, F. G. Zhang, X. H. Ji, *et al.*, *Arabian J. Chem.*, 2022, **15**, 103519–103528.
18 R. Wu, Q. C. Du, H. R. Zhang, *et al.*, *J. Saudi Chem. Soc.*, 2024, **28**, 101824–101837.
19 A. M. Dowgiallo, D. A. Guenther and J. Agric, *Food Chem.*, 2019, **67**, 12642–12651.

20 Y. Z. Wei, C. Qi, T. J. Wen, *et al.*, *Adv. Chem.*, 2017, **29**, 1366–1394.
21 L. Yang, Z. Bao, Y. Wu, *et al.*, *J. Raman Spectrosc.*, 2022, **43**, 848–856.
22 D. Han, B. Li, Y. Chen, *et al.*, *Nanotechnol*, 2019, **30**, 2067–2074.
23 L. Y. Wang, H. Chen and S. J. Ma, *Vib. Spectrosc.*, 2023, **129**, 103614–103620.
24 Z. Wang, S. Wu, L. C. Ciacchi, *et al.*, *Analyst*, 2018, **143**, 5074–5089.
25 J. Z. Yang and C. Y. Zhang, *Res. Chem. Intermed.*, 2020, **50**, 50–53.
26 Y. Lin, D. Ding, C. Hu, *et al.*, *ACS Omega*, 2021, **6**, 25996–26003.
27 L. A. Akamine, D. A. V. Medina and F. M. Lanças, *Talanta*, 2021, **222**, 121683–121692.
28 Y. Ai, P. Liang, Y. Wu, *et al.*, *Food Chem.*, 2018, **241**, 427–433.
29 Z. Lin, S. Luo, D. Xu, *et al.*, *Analyst*, 2020, **145**, 424–433.
30 A. K. Verma and R. K. Soni, *Nanotechnol*, 2019, **30**, 385502–385516.
31 Y. Ma, Y. Wang, Y. Luo, *et al.*, *J. Anal. Methods Chem.*, 2018, **10**, 4655–4664.
32 J. He, G. Song, X. Wang X, *et al.*, *J. Alloys Compd.*, 2022, **893**, 162226–162235.
33 N. Negin, F. S. Arghavan, D. Nebile, *et al.*, *Environ. Sci. Pollut. Res.*, 2021, **28**, 19222–19233.
34 R. Wu, S. Song, J. F. Lu, *et al.*, *J. Mol. Struct.*, 2023, **1278**, 134908–134914.
35 T. Kavinkumar, K. Varunkumar, V. Ravikumar, *et al.*, *J. Colloid Interface Sci.*, 2017, **4**, 1125–1133.
36 M. F. Khan, A. Jama, P. J. Rosy, *et al.*, *Inorg. Chem. Commun.*, 2022, **139**, 109422–109432.
37 W. Yu, J. Jia, J. Shi, *et al.*, *Talanta*, 2023, **254**, 124181–124193.
38 U. T. Khatoon, A. Velidandi and G. S. N. Rao, *Mater. Chem. Phys.*, 2023, **294**, 126997–127005.
39 A. Mandal, E. Dhineshkumar and T. P. Sastry, *Clean Technol. Environ.*, 2023, **1**, 1–18.
40 T. Tene, M. Guevara, F. B. Palacios, *et al.*, *Front. Chem.*, 2023, **11**, 1–14.
41 B. Das, R. Kundu and S. Chakravarty, *Mater. Chem. Phys.*, 2022, **290**, 126597–126602.
42 Y. Wang, S. Liu, Y. Hu, *et al.*, *Analyst*, 2023, **148**, 5435–5444.
43 N. Xu, Z. Tang, Y. P. Jiang, *et al.*, *J. Environ. Chem. Eng.*, 2023, **11**, 109736–109749.
44 M. Liu, X. Hu, C. Zhang C, *et al.*, *Sens. Actuators, B*, 2024, **398**, 134688–134703.
45 Y. Luo, L. Niu, Y. Wang, *et al.*, *Appl. Surf. Sci.*, 2023, **607**, 155095–155110.
46 S. Di, S. Guo, Y. Wang, *et al.*, *Mater. Chem. Phys.*, 2023, **301**, 127621–127635.
47 R. Mandavkar, S. Lin, S. Pandit, *et al.*, *Surf. Interfaces*, 2022, **33**, 102175–102189.